Journal of Environmental Chemical Engineering 11 (2023) 111343

Contents lists available at ScienceDirect

Journal of Environmental Chemical Engineering

journal homepage: www.elsevier.com/locate/jece

Enhanced removal of emerging pollutants through visible light-activated carbon nitride materials immobilized over 3D printed structures

Manuel Peñas-Garzón [a,b], Maria J. Sampaio [a,b,*], Yaidelin Manrique [a,b], Claudia G. Silva [a,b], Joaquim L. Faria [a,b]

[a] LSRE-LCM - Laboratory of Separation and Reaction Engineering – Laboratory of Catalysis and Materials, Faculty of Engineering, University of Porto, Rua Dr. Roberto Frias, 4200-465 Porto, Portugal

[b] ALiCE - Associate Laboratory in Chemical Engineering, Faculty of Engineering, University of Porto, Rua Dr. Roberto Frias, 4200-465 Porto, Portugal

ARTICLE INFO

Editor: Isabel Oller Alberola

Keywords:
Psychoactive drugs
Cylindrical support
Immobilized photocatalyst
Poly(lactic acid)
Additive manufacturing

ABSTRACT

This study investigates the performance of carbon nitride (CN) photocatalysts immobilized on 3D printed cylindrical supports for the removal of selected emerging pollutants, namely venlafaxine (VFX), citalopram (CTP), fluoxetine (FXT), and carbamazepine (CBZ), due to their rising consumption as antidepressants and the significant concerns for public health and the environment, mainly due to the direct impact of their presence in surface waters. The CN photocatalysts were synthesized using two precursors (dicyandiamide and urea), forming four different CN materials. Among the immobilized CN photocatalysts tested, the bulk CN prepared from urea (CNB-U/PLA) revealed the highest efficiency for the removal of VFX as the target antidepressant (above 90% after 30 min), which was ascribed to the lower recombination of photogenerated charges of this photocatalyst. The reuse tests confirmed the robust and effective photocatalytic performance of the CNB-U/PLA photocatalyst over multiple cycles, while its versatility with different support configurations demonstrates its adaptability and broad potential for various photocatalytic applications. The simultaneous removal of the four antidepressants was performed at low concentrations (1.8 μM), employing the most efficient immobilized photocatalyst (CNB-U/PLA), yielding remarkably high conversion rates (above 90% for VFX, CTP, and FXT, and around 70% for CBZ, after 60 min) under visible irradiation. The results demonstrate the ability of the immobilized CN system to effectively eliminate contaminants with different chemical properties. This study emphasizes the potential of this approach for comprehensive emerging pollutants removal, highlighting its significance in water treatment and environmental remediation strategies.

1. Introduction

The most prevailing mental disorders in current societies are related to depression and anxiety, affecting around 4% of the world population [1]. Regarding treatment, around 70% of depressive-related disorders are treated via the intake of antidepressants [2]. To reduce the number of side effects of the first-generation drugs, second-generation antidepressants such as serotonin and noradrenaline reuptake inhibitors (SNRIs, e.g., venlafaxine or duloxetine) and selective serotonin reuptake inhibitors (SSRIs, including citalopram, fluoxetine, and others) were developed, being currently among the most prescribed antidepressants worldwide [3]. Indeed, the average consumption of antidepressants increased by around 35% in 2010–2020 within the OECD (Organization for Economic Co-operation and Development) countries, up to 67 daily doses per 1000 inhabitants [4].

The increasing rate of consumption not only poses a severe public health problem but also directly affects the presence of pharmaceutical compounds in surface waters. These compounds are commonly detected in the range of a few hundreds of $ng \cdot L^{-1}$ to a few dozens of $\mu g \cdot L^{-1}$) [5–7]. The secondary biological treatment of these compounds in wastewater treatment plants (WWTPs) [8,9] typically fails to achieve complete elimination, with removal efficiencies averaging below 50% and even dropping below 20% for specific substances such as venlafaxine (VFX), which is currently included in the Watch List of substances for European Union monitoring [10].

Heterogeneous photocatalysis, within the advanced oxidation

* Corresponding author at: LSRE-LCM - Laboratory of Separation and Reaction Engineering – Laboratory of Catalysis and Materials, Faculty of Engineering, University of Porto, Rua Dr. Roberto Frias, 4200-465 Porto, Portugal.
E-mail address: mjsampaio@fe.up.pt (M.J. Sampaio).

https://doi.org/10.1016/j.jece.2023.111343
Received 7 July 2023; Received in revised form 9 October 2023; Accepted 26 October 2023
Available online 1 November 2023

processes, can be regarded as a promising tertiary treatment for eliminating refractory contaminants in wastewater [11,12]. In this sense, titanium dioxide (TiO_2) has been previously evaluated in the removal of antidepressant drugs (e.g., venlafaxine [13–16], fluoxetine [15–17], or sertraline [18], among others), as the preferred semiconductor due to its suitable properties for photocatalytic applications [19,20]. However, the main drawbacks of this material are mostly related to its wide band gap (E_g ~3.2 eV), restricting the light-harvesting to the UV region, as well as the use in powder form in aqueous suspensions, avoiding an easy recovery of the photocatalyst after the reaction.

A current trend in developing visible-light-responsive photocatalysts for improving light efficiency under solar irradiation or by inexpensive visible-light sources such as Light Emission Diodes (LEDs) tries to overcome the first drawback. Graphite-like carbon nitride (g-C_3N_4), based on a layered structure (similar to graphite with N atoms occupying certain C positions) of triazine or heptazine units [21], is a well-known photocatalyst active under visible irradiation (E_g ~2.7 eV). The good photocatalytic performance and physicochemical stability, together with the possibility of being prepared from different sources (e.g., dicyandiamide, urea, or melamine [22]), have promoted the use of this material for a wide range of applications (including organic synthesis [23,24], hydrogen production [25,26] or the elimination of refractory water contaminants [27,28], among others).

To mitigate the challenges associated with the separation of catalysts from treated water, techniques such as the immobilization of powdered particles onto support materials appear as a promising solution. The deposition method should be ideally easy and non-expensive to perform, durable, and inert to the reaction [29]. Over the last few years, only a limited number of works have reported using supported photocatalysts to abate contaminants of environmental concern. For example, the excellent properties of embedded TiO_2 within a polymeric framework in ablating microcystin algal toxin were recently demonstrated [30]. A recent review [31] refers to using recycled poly(ethylene terephthalate) to immobilize TiO_2, showing good performance in eliminating up to eight antibiotics. Other examples are the preparation of a graphene oxide/TiO_2 immobilized on nanofibers via electrospinning-calcination to remove propranolol [32]; or the removal of trimethoprim and quinolones using an immobilized cercosporin (a toxin with photocatalytic activity) onto a poly(methylmethacrylate) structure [33]. Concerning this investigation, the elimination of VFX (as a representative antidepressant) is hardly investigated compared to the considerable number of works reporting powder photocatalysts [13–16,34–36]. For example, some of us [37] recently described the deposition of g-C_3N_4 on a film and its use in successfully treating organic contaminants from WWTP effluents. Thus, using PVDF as the principal polymeric matrix is interesting in terms of the intrinsic properties of the resulting membrane after phase inversion. Among them, hydrophobicity, inertness, high UV resistance, or good mechanical properties, can be highlighted for photocatalytic applications [38,39]. Moreover, the operation with the PVDF solution at mild conditions of temperature and pressure may represent an advantage regarding energy consumption. Another example [15] refers to using glass rings as proper support for environmental applications. Apart from g-C_3N_4, doped-TiO_2 on glass film [40] and doped-bismuth oxyhalide anchored on alumina film [41] are among the scarce literature precedents.

In this context, the novelty of this work relies on the use of cylindrical support of poly(lactic acid) (PLA), obtained by additive manufacturing, for the immobilization of g-C_3N_4 photocatalysts (here labeled as CN) using a PVDF-based polymeric solution and their high photocatalytic efficiency in terms of antidepressants removal under visible light, easy material recovery and performance stability. The choice of PLA is supported by its accessible acquisition, easy processability, adequate mechanical properties such as stiffness (tensile modulus between polypropylene and polyethylene terephthalate) and resistance at room temperature [42], as well as low toxicity (being considered as a biocompatible material [43]). Besides, using PLA support provides a high added value to this polymer, which can be produced from biomass resources [44]. Moreover, two common CN precursors, urea, and dicyandiamide, are compared to produce the most suitable photocatalyst for removing VFX as the target contaminant. Different support configurations, such as modular features or shapes, were also investigated. The purification of a spiked water sample was examined considering the simultaneous removal of a mixture of antidepressant pharmaceuticals comprising carbamazepine (CBZ), citalopram (CTP), and fluoxetine (FXT), selected based on their potential impact on water ecosystems [7,45].

2. Materials and methods

2.1. Reagents and materials

Dicyandiamide ($C_2H_4N_4$, 99%), polyvinylpyrrolidone (PVP, > 99%), 1-methyl-2-pyrrolidone (NMP, 99.5%), poly(vinylidene fluoride) (PVDF, > 99%), venlafaxine (VFX) hydrochloride (> 99%), fluoxetine (FXT) hydrochloride (> 99%), and Nafion™ perfluorinated resin were purchased from Sigma-Aldrich. Urea (CH_4N_2O, 99.5%) was provided by Acros Organics. Citalopram (CTP) hydrobromide (> 99%) and carbamazepine (CBZ, 98%) were obtained from Supelco and Alfa Aesar, respectively. Acetonitrile (ACN, LC-MS grade) and isopropanol (≥ 99.5%) were purchased from VWR Chemicals, and formic acid (> 99.5%) was provided by Merck. Poly(lactic acid) (PLA) printer filament (1.75 mm in diameter and natural color) was purchased from FlashForge. Ultrapure (UP) water was produced in a Milli-Q water system (18.2 MΩ·cm^{-1}). Unless otherwise indicated, all experiments were performed in distilled water.

2.2. Preparation of the supported photocatalysts

2.2.1. Synthesis of the powder photocatalysts

Two distinct bulk CN (CNB) materials were synthesized via the thermal treatment of dicyandiamide (D) or urea (U). The CNB using D precursor (Fig. S1a) was prepared following a microwave-assisted polymerization procedure previously reported [22,23,37]. Briefly, 2 g of dicyandiamide were placed in a closed crucible and submitted to a heating treatment in air at 450 ºC for 0.5 h, followed by a second step at 550 ºC for 1 h using a Microwave Muffle Furnace Phoenix™ (CEM Corporative). After cooling, the resulting material was powdered in a mortar, washed with distilled water, dried overnight at 100 ºC, sieved (< 500 μm), and labeled CNB-D. For the U precursor (Fig. S1b), a similar procedure was followed using a muffle furnace (SNOL 8.2/1100), as previously described [46]. In this case, 40 g of urea in a closed crucible were heated at 450 ºC for 2 h and subsequently at 550 ºC for 4 h. To achieve the desired temperatures, a ramp of 2 ºC·min^{-1} was used in all cases. The obtained material was also powdered, washed, dried, sieved, and labeled CNB-U. As schematized in Fig. S1c, the intermediate step at 450 ºC is carried out to maximize the formation of the necessary tri-s-triazine intermediates (e.g., melem units) before the further condensation process to obtain the bulk g-C_3N_4 materials [47].

As can be observed from Fig. S1 (Supporting Information), both CNB materials were submitted to the same exfoliation process, reported elsewhere [22,37,46]. Concisely, 0.95 g were placed in an open crucible and heated at 500 ºC for 2 h (2 ºC·min^{-1}). The final material was recovered and labeled CNX-D and CNX-U, respectively, according to the precursor used.

2.2.2. Printing of PLA support

The support was prepared using a BEETHEFIRST+ 3D printer and PLA filament. The software SolidWorks (SolidWorks Corp.) was used to design the support. The support consists of a vertical column of 50.0 mm height and 36.5 mm internal diameter, as shown in Fig. S2. On the support's outer surface, 36 vertical flaps (radius of 0.9 mm) are distributed equidistantly.

2.2.3. Immobilization of the powder photocatalyst on PLA support

A polymeric solution was employed to anchor the synthesized photocatalysts onto the external surface of the support. The preparation of this polymeric solution was adapted from a previously described procedure [37,38,48]. Briefly, 0.07 g of PVP was dissolved in 6.0 mL of NMP via sonication for 3 h at room temperature. Then, 1.07 g of PVDF was added to the solution, stirring at 40 ºC for 48 h. The resulting polymeric solution was stored in a glass vial. Fig. 1 illustrates the steps followed to immobilize the photocatalyst on the support: 1) the polymeric solution, used as adherent, was added onto the external surface of the PLA support using a paintbrush to apply a thin single coating layer; 2) the photocatalyst powder was carefully dispersed; and 3) the photocatalyst/support system was dipped several times (5 times for periods of 5 min) in distilled water to promote the immobilization of the photocatalyst via phase inversion. Once dried at 30 ºC (below the glass–liquid transition temperature of PLA, $T_g \approx 60$ ºC) for 12 h, the resulting supported photocatalyst (4 ± 2% the proportion of photocatalyst in the overall mass) was finally stored until use. These photocatalysts immobilized on PLA support were labeled using the PLA suffix (e.g., CNB-D/PLA for supported CNB-D). Fig. S3 provides the final appearance of the supported photocatalysts.

2.3. Characterization of samples

A Phenom ProX instrument was used to analyze the morphology of the supported photocatalysts via scanning electron microscopy (SEM). A JASCO FT/IR-6800 equipped with a MIRacle TM single Reflection accessory was used in attenuated total reflectance (ATR) mode to determine the Fourier transform infrared (FTIR) measurements in the range of 4000–600 cm^{-1} with a resolution of 4 cm^{-1}. A Quantachrome Nova 4200e apparatus assessed the N_2 adsorption-desorption isotherms at –196 ºC. Before analysis, the samples were outgassed at 150 ºC and 40 ºC for powder and supported materials, respectively. The specific surface (S_{BET}) and the non-microporous (or external, S_{ext}) areas were estimated from the Brunauer-Emmett-Teller method [49] and t-plot method [50], respectively, whereas the amount of adsorbed N_2 at a relative pressure (P/P_0) of 0.99 was used to determine the total pore volume (V_T). Elemental analysis for determining the C/N ratio was performed in triplicate in a Vario Micro Cube analyzer at a combustion temperature of 1050 ºC. A JASCO V-560 spectrophotometer was used to examine the optical properties by ultraviolet-visible diffuse reflectance spectroscopy (UV-Vis DRS), using $BaSO_4$ as reference material. The band gap (E_g) value was estimated by the Tauc plot method [51], considering CN as an indirect semiconductor [52]. For the photoluminescence (PL) properties, a JASCO FP-8200 fluorescence spectrometer equipped with a 150 W Xenon lamp was used. The excitation wavelength was set at 370 nm, with both the excitation and emission bandwidths of 2.5 nm. A Zahner Zennium electrochemical workstation was used to obtain the Motts-Schottky plots. The measurements were made in a three-electrode open cell (working electrode: fluorine-doped tin oxide glass coated with a suspension of the selected photocatalyst; counter electrode: Pt wire; reference electrode: Ag/AgCl, 3 M KCl). The electrolyte was a 0.1 M Na_2SO_4 (pH 6.3) aqueous solution, deaerated with argon prior to each analysis. Each photocatalyst suspension was prepared following a methodology previously described [53], consisting of mixing 1 mL of distilled water, 250 µL of isopropanol, 50 µL of Nafion solution, and adding 5 mg of the catalyst. The mixture was submitted to ultrasounds for 30 min to obtain a homogeneous suspension, then deposited on the working electrode by a drop-casting method (drying step at 80 ºC). Mott-Schottky plots were recorded by varying the applied potential from − 1.5–1.0 V vs. Normal Hydrogen Electrode (NHE), using a frequency of 1 kHz and an amplitude of 50 mV. The semiconductor flat band potential, V_{FB}, was estimated following the Mott–Schottky equation (Eq. 1) [54]:

$$\frac{1}{C^2} = \frac{2}{\varepsilon \cdot \varepsilon_0 \cdot e \cdot N_D} \cdot \left(V - V_{FB} - \frac{k \cdot T}{e} \right), \quad (1)$$

Backspace

being C the capacitance at target voltage V; ε represents the semiconductor permittivity and ε_0 the void permittivity; e the electron charge; k the Boltzmann's constant; and T the temperature. The conduction band potential (V_{CB}) is calculated following the Nernst equation at pH 7 (Eq. 2)[55]:

$$V_{CB} = V_{FB(Ag/AgCl,\ NHE,\ pH)} - 0.059 \cdot (7 - pH)\ , \quad (2)$$

Eventually, Eq. (3) allows to estimate the valence band potential (V_{VB}):

$$V_{VB} = V_{CB} + E_g/e\ , \quad (3)$$

where E_g is the bandgap of the semiconductor. For all supported materials, the analyses were assessed in (at least) three different areas of the surface to obtain a representative result.

2.4. Photocatalytic setup and analytical techniques

The photocatalytic performance of the different synthesized materials was first evaluated for removing VFX (unless otherwise indicated, 5 $mg \cdot L^{-1}$) as a target antidepressant in distilled water under visible light. The removal of other pharmaceuticals from the psychoactive drug family, namely CBZ, CTP, and FXT, both individual (5 $mg \cdot L^{-1}$) and in the mixture (1.8 µM each one, corresponding to a concentration of VFX of 0.5 $mg \cdot L^{-1}$) was also evaluated. As schematized in Fig. 2**a**, a borosilicate glass reactor containing 120 mL of distilled water spiked with the contaminant was placed inside an LED box equipped with four perpendicular visible LEDs (average nominal irradiance = 560 $W \cdot m^{-2}$, λ_{max} = 414 nm and full width at half maximum (FWHM) = 25 nm, Fig. 2**b**) located at 3 cm from the reactor wall. An OceanOptics USB2000 + spectroradiometer was used to characterize the LEDs. The borosilicate glass reactor was equipped with an internal glass cylinder that enables the cooling of the reaction medium (experiments temperature ~20 ºC) and allows the supported photocatalyst to be fixed in the center of the reactor without interacting with the reactor wall and being equidistant from the LEDs (Fig. 2**c**). The solution was stirred and

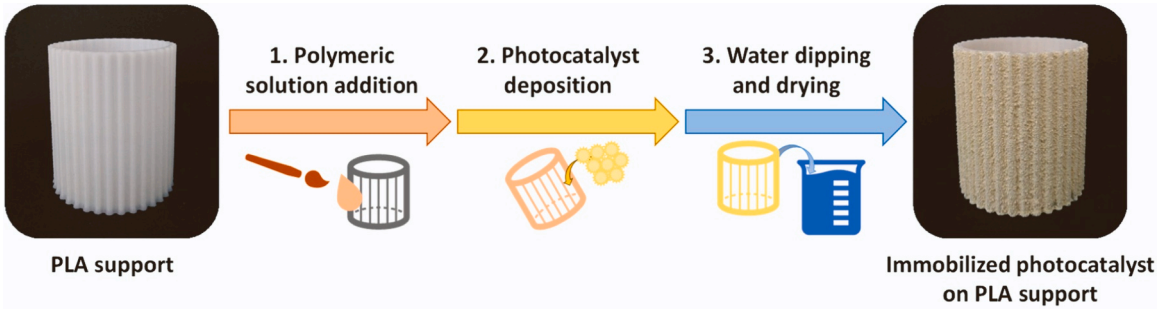

Fig. 1. A schematic representation of the sequential steps involved in immobilizing CN materials onto the cylindrical PLA support using a polymeric solution.

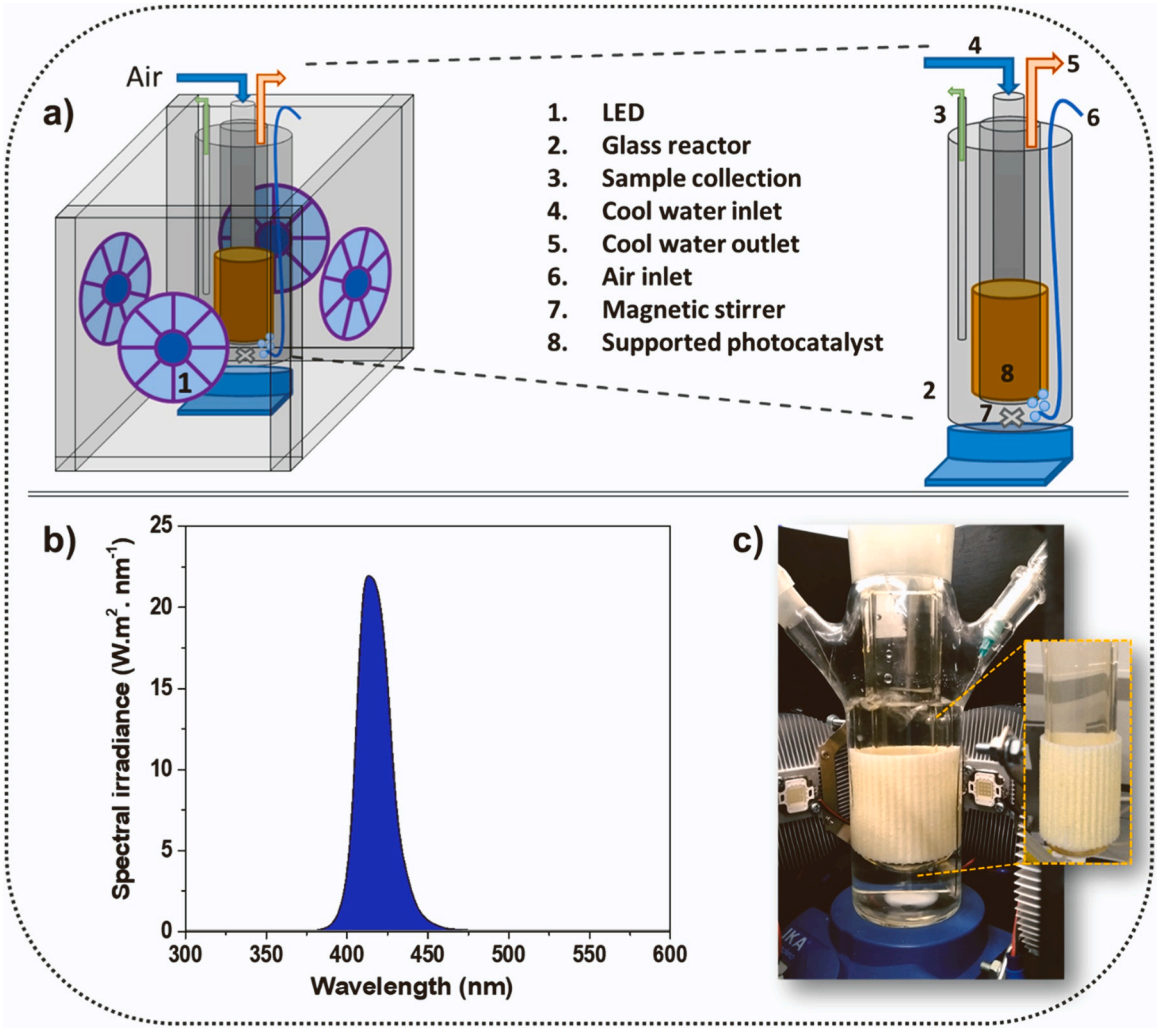

Fig. 2. a) Scheme of the experimental setup; b) average spectral irradiance of the LEDs; c) image of the photocatalytic reactor inside the LEDs system.

saturated with air (~50 mL·min^{-1}, using an air pump) throughout the experiments. Some preliminary experiments used CN suspensions (1.0 g·L^{-1}). Before the beginning of the irradiation, the contaminant solution and the photocatalyst were left in the dark under stirring for 60 min to achieve the adsorption equilibrium. The VFX conversion stability was tested with the supported photocatalyst with the best photocatalytic performance. After each cycle, the supported photocatalyst was washed with distilled water and dried (40 ºC for 12 h). All experiments were duplicated, and average values were included. A third experiment was performed in case of more than a 3% difference in the duplicates.

The evolution in the contaminant concentration was monitored by Ultra High-Pressure Liquid Chromatography (UHPLC). A Nexera X2 LC-30AD apparatus was used with an RF-20Axs Fluorescence detector (FD) and an SPD-M20A diode array detector. A Kinetex™ XB-C18 100 Å reverse phase column (100 × 2.1 mm i.d., 1.7 µm particle diameter) was used with a mobile phase (0.25 mL·min^{-1} at 30 ºC) composed of 0.1% formic acid aqueous solution/ACN (A/B). The antidepressants VFX, CTP, and FXT were detected by fluorescence (λ_{exc} = 230 nm, λ_{emi} = 300 nm) using isocratic methods (A/B = 77/23% v/v for VFX and CTP, and A/B = 67/33% v/v for FXT), while the diode array detector (λ = 286 nm) was required for CBZ (isocratic methods of A/B = 65/35% v/v), respectively. A gradient method was employed to detect all the pharmaceuticals when used in a mixture, wherein the concentration of ACN varied from 23% to 33%. The apparent pseudo-first-order rate constant, k_{app} (min^{-1}), was estimated through the equation: $ln\ (C_0/C_t) = k_{app} \times t$, where C_0 and C_t are the concentrations at irradiation times 0 and t, respectively. The half-conversion time ($t_{1/2}$) was estimated considering $C_t = C_0/2$. The identification of the main short-chain carboxylic acids (using corresponding standards solutions) formed during the conversion of the contaminants was performed using a Hitachi Elite LaChrom instrument equipped with an L-2400 UV detector (λ = 200 nm), and a Hichrom Alltech 0A-1000 column (300 mm × 6.5 mm). A solution of 5 mM H_2SO_4 (0.5 mL·min^{-1}) was used as the isocratic mobile phase.

3. Results and discussion

3.1. Characterization of the supported photocatalysts

The main characterization of the CN photocatalysts (powder form) was comprehensively analyzed in previous works of our research group [15,22,46]. Thus, the characterization included in this study aims to confirm if the supported materials maintain the main chemical, morphological, and optical properties.

Fig. 3 shows the SEM images of the different synthesized CN deposited on the PLA support. Comparing the cross-section micrographs of the immobilized photocatalysts to the neat PLA support (Fig. 3**a**), it can be observed that the CN particles are successfully anchored over the surface, showing different thicknesses among materials. Indeed, the average photocatalyst thickness (Table S1) ranges from around 105–70 µm in bulk (Fig. 3**b-c**) and exfoliated (Fig. 3**e-f**) samples,

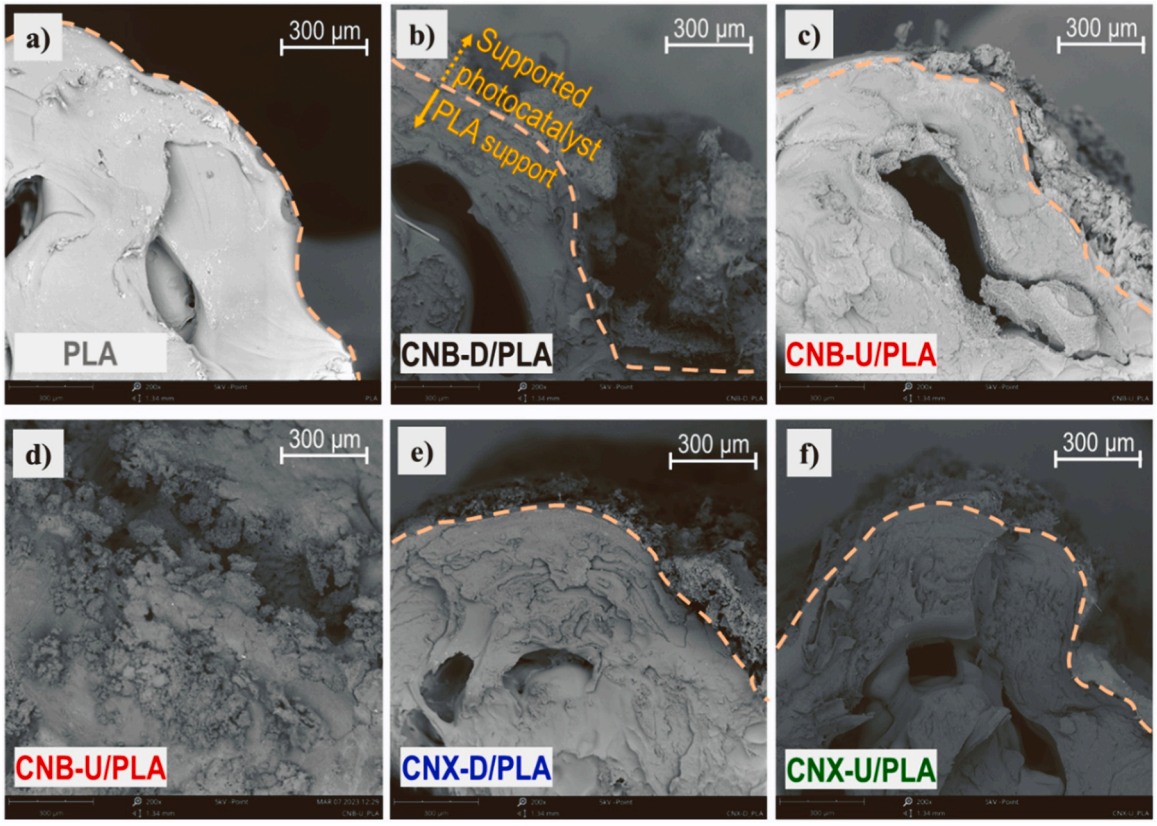

Fig. 3. SEM images of the cross-sectional of neat PLA (a), the supported photocatalysts (a, b, c, e, and f), and a front view image of CNB-U/PLA (d).

respectively. As previously reported, these differences can be directly related to the extent of the exfoliation degree (and, therefore, other properties such as density) [46]. The CN sheets tend to stack, forming compact aggregates in the bulk materials, whereas thinner plates are formed after the delamination process during the exfoliation step.

Regarding the precursor used, the formation of CN sheets with a higher disorder degree occurs when using urea compared to the counterpart using dicyandiamide [22]. These observations are coherent with the morphology of the prepared supported materials depicted in Fig. 3 and those of the frontal view micrographs collected in Fig. S4. The characteristic PLA layers, resulting from the 3D printing via additive manufacturing, can be observed in Fig. S4a, in contrast to the other

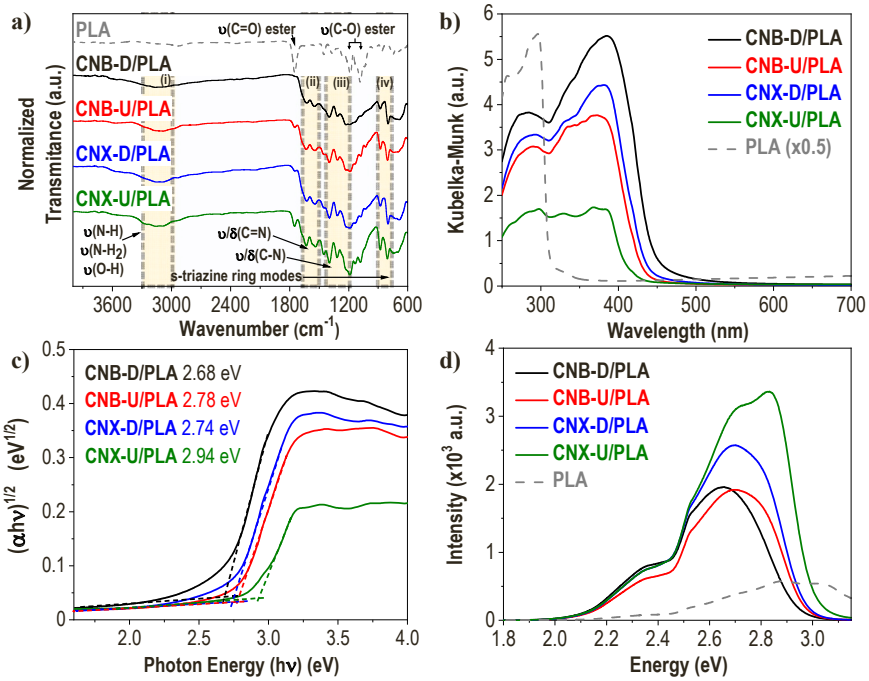

Fig. 4. a) FTIR-ATR; b) UV-Vis DRS; c) Tauc plot; and d) PL spectra of the supported photocatalysts. PLA support was also included for comparison.

micrographs in which the photocatalyst particles are well-distributed, covering the surface of the support (Fig. 3d and Figs. S4b-e).

The powder materials show higher development of the porous texture (as can be seen in Fig. S5 and Table S2), depicting type II isotherms with H3 hysteresis loops, typical of mesoporous plate-like particles, in agreement with some previously reported studies [22,46,56]. According to Fernandes *et al.* [23], the porous texture of these materials is mainly ascribed to the interstitial distance between CN layers due to the absence of surface pores. Indeed, it is important to remark on the increment of the S_{BET} areas of CNX samples in our study, related to the separation of sheets during the thermal exfoliation, as well as the higher specific area of urea-based materials, probably ascribed to the intermediate generation of gas bubbles (e.g., from the release of CO_2) during the polymerization synthesis step [57,58]. However, it is also interesting to note that these textural differences of the powder CN are practically hindered once the materials are supported, probably due to the non-porous character of the PLA support ($< 1\ m^2 \cdot g^{-1}$) and the mass proportion of photocatalyst in the overall supported sample.

Regarding the chemical structure of the supported photocatalysts, the FTIR-ATR analysis (Fig. 4**a**) shows four different regions, suggesting the presence of graphite-like sp^2 structures [59–61]: (i) the first band centered around 3150 cm^{-1}, corresponding to the stretching vibrations of N–H and N–H_2 and remaining adsorbed water molecules. The bands corresponding to stretching and bending vibrations of C=N appear at ca. 1630 and 1545 cm^{-1} (ii) and C-N at 1398, 1316, and 1228 cm^{-1} (iii), respectively. The two bands centered ca. 880 and 804 cm^{-1} (iv) are commonly ascribed to the vibration modes of s-triazine units [60,62]. Compared to the powder photocatalysts (Fig. S6), it can be observed a general reduction in the transmittance intensity (expected after the particles anchoring), but maintaining the main chemical structures, indicating that the supporting process does not affect the chemical structure of the photocatalysts, in agreement with the previous work of Sampaio *et al.* [37]. Besides these regions, some new bands can be identified from Fig. 4**a** in the supported samples related to the presence of the PLA. That is the case of the three bands with higher intensity centered around 1750, 1184, and 1082 cm^{-1}, which can be ascribed to the stretching vibrations of the ester groups (mainly –C=O and –C–O) within the aliphatic polyester PLA structure [63]. Those bands are present in all supported photocatalysts, again proving the intimate contact between photocatalyst particles and support. The transmittance intensity of those characteristic PLA bands is reduced by increasing the above-mentioned average photocatalyst thickness on the surface of the samples, which can be explained by considering the ATR analysis assessed.

The light absorption profiles of the supported CN samples are depicted in Fig. 4**b**. It can be observed that the bulk materials present higher absorption compared to the exfoliated counterparts, which show a hypsochromic shift of around 10 nm, usually attributed to changes at the electronic level due to the modification in the interaction among aromatic structures after exfoliation [64], also causing a slightly paler color of the samples, even perceptible at the macroscopic scale (as previously shown in Fig. S3). The broad lower light absorption of urea-based materials can be ascribed to the more significant sheets disorder, as previously reported [22], and a higher atomic C/N ratio (as summarized in Table S2), probably due to the creation of N vacancies. Generating these nitrogen vacancies may allow the formation of defects in the CN sheets, resulting in different optoelectronic properties [23,65]. In general, all supported photocatalysts show maximal absorbance in the region ca. 365–385 nm, with intensity absorption above 50% up to 400–425 nm and band gap energies in the range of ca. 2.7–2.9 eV (estimated from the respective Tauc plots, Fig. 4**c**). In addition, the obtained band gap values are consistent with previously reported findings regarding preparing similar materials [46,56,66].

It is noteworthy to observe the influence of PLA support depicted in Fig. 4**b**, wherein a prominent absorption band is observed within the 250–300 nm range, accompanied by increasing absorption tails in the visible region (referred to as Urbach tails). These spectral characteristics are likely attributed to the amorphous nature of the polymeric structure resulting from the extrusion process during 3D printing [67]. Compared to the powder samples (Fig. S7), it can be inferred that the increased absorption profile observed in the supported photocatalysts can be ascribed to PLA support. However, this increment in the light absorption does not interfere with the band gap values. As can be observed from Fig. S8, the supported photocatalysts present the same band gap values as the powder materials, as expected, due to the simple deposition step used to anchor the photocatalyst particles on the support.

The PL emission spectra shown by the supported photocatalysts (Fig. 4**d**) depict the characteristic profiles of CN-related materials: maxima emission around 2.65–2.70 eV (being ca. 2.84 eV for CNX-U sample), followed by two shoulders shifted to lower energies (placed ca. 2.4 and 2.5 eV). The maxima PL intensity corresponds to the energy emitted after electron-hole recombination in these materials [46,68] and the other emission bands related to intermediate energy states and defects acting as centers of lower energy transitions [69,70]. It can be observed that the powder samples (Fig. S9) depict similar PL profiles in all cases with higher intensities. Coherently with previous CN-related supported materials [37], the reduced PL intensity of supported photocatalysts in this study can be explained as a consequence of the interference with the PLA support instead of a quenching effect due to lower recombination of photogenerated charges. Regardless of the support presence, the exfoliated materials show higher PL intensity, in agreement with the degree of structural and surface defects (which can act as recombination centers [23,71]) due to the thermal preparation step.

The higher degree of structural defects of exfoliated samples can also be observed at the electronic scale, as can be rationalized from the estimated band configurations. The Mott–Schottky equation (Eq. 1) was used to determine the V_{FB} for each powder material through the intercept point of the tangent line with the V-axis in the Mott–Schottky plot (Fig. S10a). Subsequently, the CB potential levels were estimated (Eq. 2) to be located at − 1.01 (CNB-D), − 1.07 (CNB-U), − 1.17 (CNX-D), and − 0.97 V (CNX-U), respectively, in agreement with similar g-C_3N_4-based materials [22]. Finally, the potential for the valence bands was calculated following Eq. (3), being the values of V_{VB} shown in Fig. S10b, in which the plausible band configuration for each synthesized material is proposed.

3.2. Photocatalytic performance of supported photocatalysts

3.2.1. Effect of the precursor and photocatalyst stability

The photocatalytic performance of the supported photocatalysts in converting venlafaxine (VFX) under visible irradiation is depicted in Fig. 5**a**. Control experiments, including the photolytic removal of VFX, as well as using the bare cylindrical support with and without the polymeric film (used to anchor the photocatalyst), were also evaluated (Fig. S11a). The results revealed high photochemical stability of the contaminant in the absence of the photoactive phase (CN materials), which was expected since VFX does not absorb the emission band of the light source used ($\lambda_{max} = 414$ nm). Besides, it can also be observed that the adsorption of the contaminant on the photocatalyst surface can be considered negligible (below 3%). Fig. 5**a** shows that, under visible irradiation, VFX is completely removed in 60 min, achieving conversion values ca. 80% after the first 20 min of photocatalytic treatment using the supported materials CNB-U/PLA, CNX-D/PLA, and CNX-U/PLA.

On the other hand, using the CNB-D/PLA (D bulk material), a decrease in the removal rate was observed (Fig. 5**a**). The better photocatalytic performance of exfoliated CN has been previously related to the higher porous development (and thus, better contact with contaminant) of these materials compared to the bulk counterpart [22,46]. Comparison experiments using powder photocatalysts (Fig. S11b) exhibit two interesting features: i) faster removal rates of the contaminant compared to supported materials, which was expected due to the higher exposed

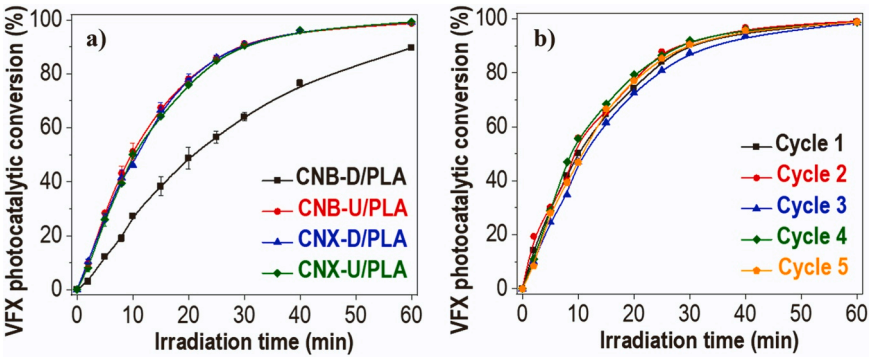

Fig. 5. Photocatalytic conversion of VFX under LED irradiation using a) supported photocatalysts and b) CNB-U/PLA under consecutive reuses. $[VFX]_0 = 5\ mg{\cdot}L^{-1}$; LED λ_{max}= 414 nm; Irradiance = 560 $W{\cdot}m^{-2}$.

photocatalytic area of the non-supported samples, and ii) the resemblance between the trend of bulk and exfoliated materials compared to the results shown by the supported photocatalysts. At this latter point, it should be remarked that the almost similar performance displayed by the supported CNB-U/PLA compared to the supported exfoliated samples, CNX-D/PLA and CNX-U/PLA. Therefore, it can be inferred that some properties of the supported CNB-U photocatalyst may allow it to perform a comparable conversion of the target contaminant. The lower

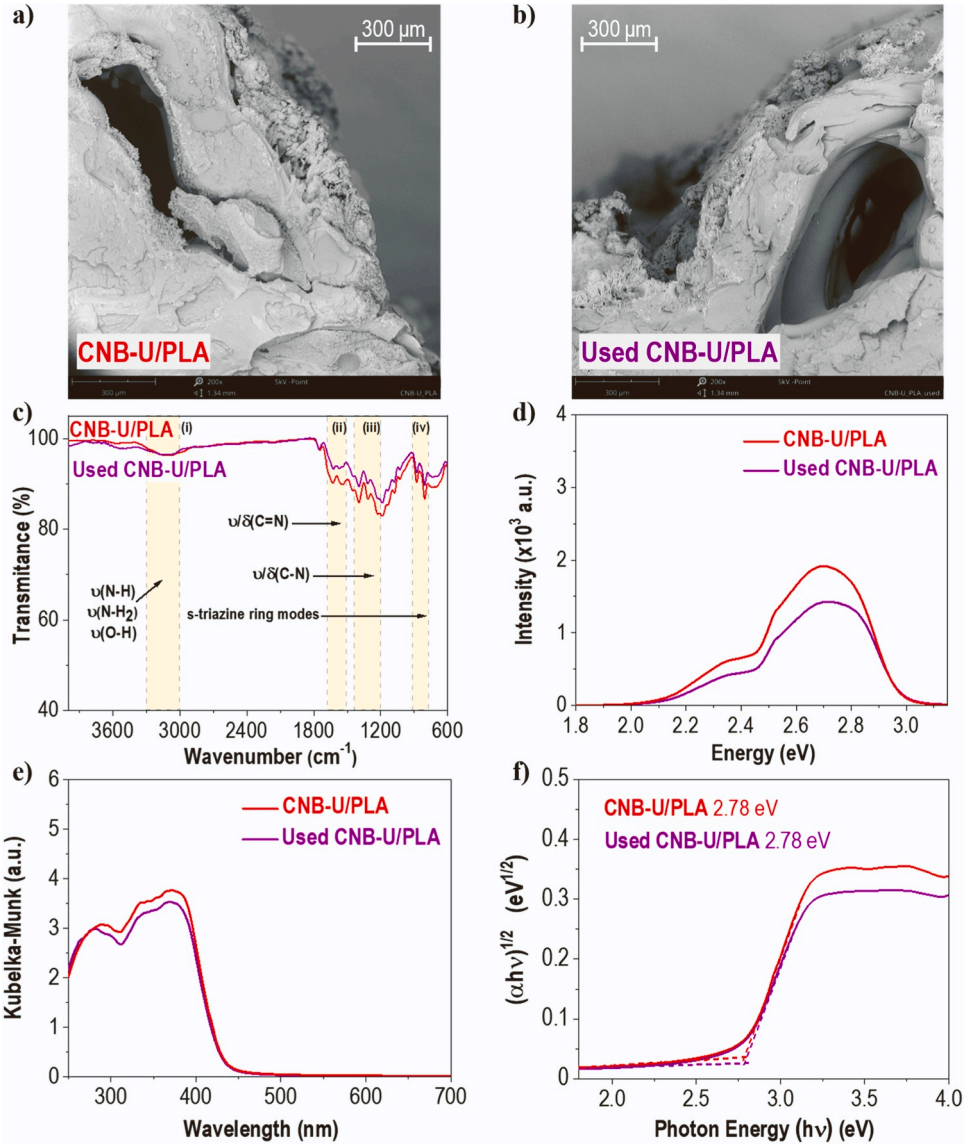

Fig. 6. SEM images of as-prepared (a) and used CNB-U/PLA (b). Characterization of as-prepared and used CNB-U/PLA: c) FTIR-ATR; d) PL; e) UV-Vis DRS spectra; and f) Tauc plot.

development of the porous texture in CNB-U compared to exfoliated materials seems to be overcome by lower recombination of photogenerated charges, according to the lower PL profile, as previously discussed in the characterization results. Besides, and regarding the photocatalyst preparation, it is important to note the lack of necessity of driving the exfoliation step when using urea as a CN precursor due to the similar photocatalytic performance. Furthermore, examining the similar VFX conversion profile of CNB-U and CNX-D, it is highly recommended to consider more appropriate the first photocatalyst, considering two important aspects: i) a lower number of synthesis stages and ii) the least expensive character of urea (which can be obtained from biomass resources [72]) compared to dicyandiamide.

Once the CNB-U/PLA sample was selected as the right supported photocatalyst, the stability of the performance was assessed. Fig. 5**b** shows that the photocatalytic conversion profiles of VFX using CNB-U/PLA remain nearly constant after five consecutive reuses. Indeed, when evaluating only the initial 30 min of the reaction, the conversion of the antidepressant drug was kept around 90 ± 2% within the different reuse cycles. It is also important to highlight the main benefits of supported photocatalysts regarding the recovery of the photocatalysts after the reaction. In this sense, the novel system presented of CNB-U supported on PLA, in addition to maintaining the photocatalytic performance, allows a simple set-and-use approach. The straightforward procedure consists of placing the supported sample in the reaction system, using it throughout the required photocatalytic time, and finally collecting the supported photocatalyst for new uses. Conversely, using a powder photocatalyst (Fig. S12) requires separating the suspended solid material from the aqueous solution using mechanical approaches such as filtration and centrifugation. Besides, it should be also remarked that the use of the same supported photocatalyst represents another important advantage considering the savings in fresh powder photocatalyst for each new experiment.

The characterization of the resulting CNB-U/PLA after consecutive use, including most experiments reported in this study (with a total service time of around 30 h), is shown in Fig. 6. The slight difference observed between the unused and used CNB-U/PLA may infer that a minor part of the photocatalyst was partially lost, probably by expected attrition after several uses, manipulation, and washing steps. These variations can also be due to the characterization measurements at slightly different points of the supported photocatalysts.

Comparing the results obtained in the present study with those reported in the literature for the degradation of VFX is wide challenging due to the variable operation parameters used in each study, as summarized in Table 1. As mentioned previously, few works have documented the use of immobilized photocatalysts for water/wastewater treatment [15,37,40,41]. For example, some of us studied the use of a polymeric film for the degradation of a mixture of VFX and metoprolol using a similar experimental setup [37]. Although in that work quite promising results for the degradation of several micropollutants found in wastewater were obtained, the versatility of the immobilized film remained to be investigated, which holds significant importance when considering its potential for pilot-scale growth. Therefore, in the present study, the evaluation of the photocatalytic performance was followed by the evaluation of different support configurations, including modular features or shapes as discussed below. Regarding the activity in the removal of the target antidepressant, the immobilized photocatalysts employed in our study show auspicious performance under visible light. Indeed, the apparent pseudo-first-order disappearance rate constant (k_{app}) displayed by the CNB-U/PLA sample (7.54×10^{-2} min^{-1}, corresponding to $t_{1/2}$ = 9.2 min) can be considered comparable, or even higher, to the other non-supported photocatalysts collected in Table S3. Focusing on supported materials, Mokhtari et al. [40] recently investigated the removal of VFX using Ag-doped TiO_2 immobilized on glass slides under visible light, being reported a value of k_{app} ($0.76\times10^{-2}min^{-1}$, $t_{1/2}$ = 91.2 min) around an order of magnitude lower compared to the counterpart estimated for the CNB-U/PLA in this study. Another supported photocatalyst, Bi(0)-doped bismuth oxyhalide films [41] proved to remove VFX (around 60% after 60 min) in a mixture with other organic pollutants under solar light. In this respect, the absence of metallic elements in the photocatalysts described in our study represents an important advantage concerning the likely release of metals into the treated waters.

3.2.2. *Different configurations of the supported photocatalyst*

One important consideration regarding the potential utilization of the designed photocatalyst structures is to evaluate its modular character, i.e., the feasibility of being used within different sizes. Thus, it can be ideally scaled up to higher or smaller systems. In this sense, Fig. 7**a** displays the evolution of the photocatalytic removal of VFX using the standard PLA support and extra support with ½ of the height (i.e., 5.0 and 2.5 cm within the longitudinal axis of the PLA support, respectively, as can be seen from Fig. S13, keeping constant the rest of the parameters). As expected, the reduction in the height of the support (and consequently, the decrease of the available photocatalyst area) resulted in a reduction of the VFX conversion rate (even though achieving removal of ca. 90% after 60 min, two-fold the time required when using

Table 1
Removal of VFX using supported current and literature photocatalysts.

	Photocatalyst	Light source	Parameters (V =VFX,Ph = Photocatalyst)	% Photocatalytic removal /k_{app} ($\times10^{-2}min^{-1}$) / $t_{1/2}$ *(min)*	Ref
Supported photocatalysts	CNB-D/PLA	Visible light(LED, 414 nm, 560 $W{\cdot}m^{-2}$)	$[V]_0 = 5\ mg{\cdot}L^{-1}$	91.1% (60 min) /3.65 / 19.0	This work
	CNB-U/PLA	Visible light(LED, 414 nm, 560 $W{\cdot}m^{-2}$)	$[V]_0 = 5\ mg{\cdot}L^{-1}$	98.7% (60 min) /7.54 / 9.2	This work
	CNX-D/PLA	Visible light(LED, 414 nm, 560 $W{\cdot}m^{-2}$)	$[V]_0 = 5\ mg{\cdot}L^{-1}$	99.1% (60 min) /7.68 / 9.0	This work
	CNX-U/PLA	Visible light(LED, 414 nm, 560 $W{\cdot}m^{-2}$)	$[V]_0 = 5\ mg{\cdot}L^{-1}$	99.2% (60 min) /7.45 / 9.3	This work
	CNB-U/PLA	Visible light(LED, 414 nm, 560 $W{\cdot}m^{-2}$)	$[V]_0 = 0.5\ mg{\cdot}L^{-1}$ *(Pharmaceuticals mixture)*	98.8% (60 min) /6.57 / 10.6	This work
	Exfoliated g-C_3N_4/PVDF film	Visible light(LED, 417 nm, ~350 $W{\cdot}m^{-2}$)	$[V]_0 = 0.25\ mg{\cdot}L^{-1}$ *(Pharmaceuticals mixture in WW)*	100% (150 min) */n.r.*	[37]
	Exfoliated g-C_3N_4/glass rings	Visible light(LED, 417 nm, ~450 $W{\cdot}m^{-2}$)	$[V]_0 \approx 4{\cdot}10^{-4}\ mg{\cdot}L^{-1}$ *(Pharmaceuticals mixture in WW)*	~45% (c.m.) */n.r.*	[15]
	Ag-TiO_2/glass film	Visible light(LED, *n.r.* nm, *n.r.* $W{\cdot}m^{-2}$)	$[V]_0 = 5.0\ mg{\cdot}L^{-1}$	~75% (180 min) /0.76 / 91.2	[40]
	Bi-doped $BiOCl_{0.875}Br_{0.125}$ / alumina film	Simulated solar light(> 280 nm, 500 $W{\cdot}m^{-2}$)	$[V]_0 = 0.1\ mg{\cdot}L^{-1}$ *(Pharmaceuticals mixture)*	~60% (60 min) */n.r.*	[41]

k_{app}: apparent pseudo-first-order rate constant; $t_{1/2}$: half-conversion time; n.r.: not reported; c.m.: continuous mode; WW: wastewater. Since different experimental conditions were used, the data in this Table is provided to summarize relevant studies and not to compare the results between them.

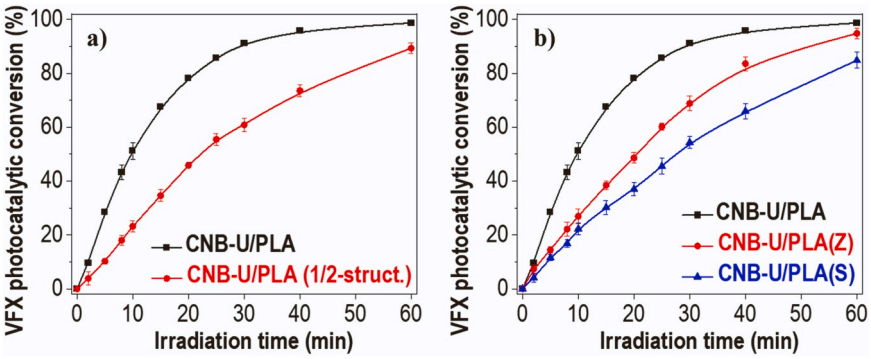

Fig. 7. Photocatalytic conversion of VFX under LED irradiation using CNB-U immobilized on a) standard and ½ PLA support and b) different PLA support configurations of PLA support. $[VFX]_0 = 5\ mg{\cdot}L^{-1}$; LED λ_{max}= 414 nm; Irradiance = 560 $W{\cdot}m^{-2}$.

the standard CNB-U/PLA sample). Indeed, the pseudo-first-order kinetic constant reduced by around 55% its value ($k_{app} = 3.44{\times}10^{-2}\ min^{-1}$) when the half-structure was used under the same reaction parameters, thus proving the modular character of the prepared supported photocatalyst.

Besides the height of the support, different configurations (i.e., twist torsional angles of the original vertical flaps) of the PLA support were also investigated. As shown in Fig. S14, two opposite shapes, namely Z- or S-configuration (when the upward direction of support flaps follow a twist angle of +180º or −180º, respectively, considering + the counterclockwise twist), were evaluated. According to the profiles displayed in Fig. 7**b**, it can be identified that the CNB-U/PLA (in which the flaps are vertically straight distributed) presents the most suitable performance for VFX conversion. This behavior can be explained by considering the orthogonal arrangement (90º) between the vertical flaps and the rotation of the aqueous solution (mainly in the horizontal plane), maximizing the photocatalyst-contaminant contact.

3.2.3. *Photocatalytic conversion of different antidepressant pharmaceuticals*

Once proved the possibilities of the CNB-U/PLA on the photocatalytic removal of VFX as a target antidepressant, the study was followed to investigate the performance of the removal of other pharmaceuticals, usually consumed to treat depression and anxiety episodes. Carbamazepine (CBZ), citalopram (CTP), and fluoxetine (FXT) were selected as target pollutants, whose main pharmacological applications and structural differences are summarized in Table S4. From Fig. 8**a**, it can be observed that each antidepressant compound is practically eliminated from the solution in less than 2 h under visible irradiation. As previously monitored for VFX, comparison experiments using the non-supported materials and photolysis tests were assessed for the rest of the contaminants (Fig. S15), as expected negligible conversion in the absence of photocatalyst was detected. To investigate the efficiency of the supported photocatalyst and assess performance with more accurate contaminant parameters, the conversion of all compounds within a mixture was examined (Fig. 8**b**) using equimolar concentration (1.8 μM, approximately 0.5 $mg{\cdot}L^{-1}$ of VFX). Despite the presence of the other pharmaceuticals, an apparent similarity can be observed between the individual and the mixture of contaminants, yielding the total degradation of compounds with differences in their chemical structure, as in the case of VFX, CTP, and FXT. On the other hand, a lower conversion tendency was displayed by CBZ, probably ascribed to a superior refractory character for the breakdown of the olefinic double bond on the central heterocyclic ring, as previously described by Rao *et al.* [73].

A remarkable similarity among the kinetic constant values was registered (Table 2) considering the individual and the concomitant removal of antidepressants. Only a minor decrease in the k_{app} values was observed, probably due to a competitive reaction between the contaminants, although a slight increment was found for FXT. That positive effect could be related to a better interaction with photogenerated oxidant species due to the lower initial concentration of contaminants.

Table 2
Values of the apparent pseudo-first-order rate constant of the antidepressive pharmaceutical compounds investigated in this study using CNB-U/PLA.

Antidepressive pharmaceutical	k_{app} ($\times10^{-2}\ min^{-1}$)	
	Individual treatment	Mixture treatment
VFX	7.54	6.57
CBZ	1.43	1.40
CTP	4.31	4.19
FXT	2.69	3.56

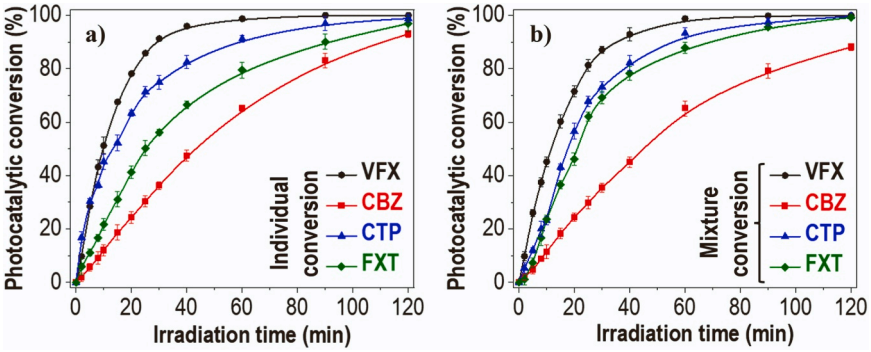

Fig. 8. Photocatalytic conversion of VFX, CBZ, CTP, and FXT under LED irradiation using CNB-U/PLA. The removal of the antidepressant pharmaceuticals was evaluated: a) individually ($[contaminant]_0 = 5\ mg{\cdot}L^{-1}$), and b) in mixture ($[contaminant]_0$ = 1.8 μM (each one), approx. 0.5 $mg{\cdot}L^{-1}$ VFX). LED λ_{max}= 414 nm; Irradiance = 560 $W{\cdot}m^{-2}$.

Overall, these results demonstrate the appropriate behavior of the supported CN photocatalyst for the abatement of a mixture of antidepressants at concentrations closer to actual environmental conditions.

Indeed, a likely oxidation mechanism for the degradation of these antidepressants using the CNB-U/PLA can be proposed according to the band configuration determined by electrochemical characterization (Fig. S10b). As schematized in Fig. 9, the illumination of the photocatalyst using visible irradiation (as LED lights used in this study) can induce the separation of charge carriers (e^-/h^+), responsible for the generation of reactive oxygen species (ROS, such as hydroxyl radical, $HO^\bullet$; and superoxide radicals, $O_2^{\bullet-}$). It is interesting to note that, according to the potential level of the CNB-U valence band, the generation of $HO^\bullet$ from direct oxidation of water molecules is energetically prevented (+2.29 V vs NHE at pH 7 [74]). Therefore, it can be rationalized that the conversion of the target antidepressants may occur by the interaction with $O_2^{\bullet-}$ or via direct oxidation with the photogenerated h^+. The conversion of these contaminants could allow the generation of intermediates and the final mineralization into harmless inorganic compounds. In this respect, some intermediate byproducts, such as diverse carboxylic acids (up to six different short-chain compounds) were identified by HPLC (Table S5). Among them, fumaric, oxamic, and oxalic acids were simultaneously identified as degradation intermediates for the four antidepressants. On the other hand, pyruvic acid was identified in the degradation of VFX, CBZ, and CTP, whereas acetic acid was detected during the conversion of VFX and CBZ, and formic acid was found only for VFX and FXT. It can also be observed from Table S5 that the area registered for most of the detected carboxylic acids decreased during the evolution of the reaction, indicating an adequate removal of these byproducts and confirming the conversion process of the antidepressants investigated in this study.

4. Conclusions

The successful immobilization of CN on cylindrical poly(lactic acid) supports was accomplished using a polymeric solution, resulting in immobilized photocatalysts with excellent photocatalytic performance for removing antidepressants under visible irradiation.

The properties of CN (mainly textural, optical, and electronic ones) depend on the precursor and the number of thermal stages followed in preparing the photocatalyst.

Regarding the photocatalytic performance under LED light, the bulk CN prepared from urea displayed similar conversion trends compared to the exfoliated photocatalysts, with almost complete conversion of the target pharmaceutical after a few minutes of treatment. The immobilized photocatalyst proved to be highly efficient in removing a mixture of antidepressants within a short period, demonstrating its effectiveness in efficiently degrading compounds with different chemical structures. Up to six different short-chain carboxylic acids (fumaric, pyruvic, oxamic, oxalic, acetic, and formic acids) were identified as likely intermediates in the conversion process for each contaminant.

Concerning the potential application, the immobilized photocatalyst depicted an adequate preservation of the photocatalytic conversion and properties after consecutive use and demonstrated the ability to operate modular-like systems. The simple set-and-use feature and the outstanding photocatalytic performance under visible light contribute to the conclusion that the supported photocatalyst represents a promising approach for its further environmental application in the elimination of refractory contaminants as antidepressant pharmaceuticals.

CRediT authorship contribution statement

Manuel Peñas-Garzón: Conceptualization, Methodology, Formal analysis, Writing – original draft. **Maria J. Sampaio:** Conceptualization, Methodology, Visualization, Writing – review & editing. **Yaidelin Manrique:** Formal analyses. **Claudia G. Silva:** Funding acquisition, Writing – review & editing. **Joaquim L. Faria:** Conceptualization, Funding acquisition, Writing – review & editing.

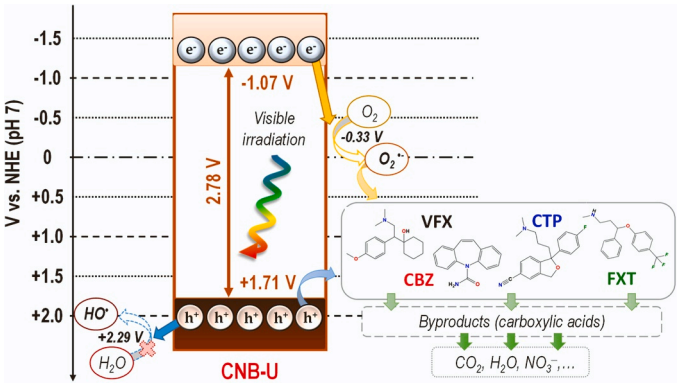

Fig. 9. Proposed photocatalytic mechanism for the antidepressants removal under visible irradiation using CNB-U/PLA.

Declaration of Competing Interest

The authors declare that they have no known competing financial interests or personal relationships that could have appeared to influence the work reported in this paper.

Data Availability

Data will be made available on request.

Acknowledgments

This work was financially supported by LA/P/0045/2020 (ALiCE), UIDB/50020/2020, and UIDP/50020/2020 (LSRE-LCM), funded by national funds through FCT/MCTES (PIDDAC). The authors also thank the project ClimActic (NORTE-01-0145-FEDER-000071). M. Peñas-Garzón acknowledges the postdoctoral fellowship from Fundación Ramón Areces (XXXIV Convocatoria Ciencias de la Vida y de la Materia). MJS acknowledges FCT funding under the Scientific Employment Stimulus - Institutional Call (CEECINST/00010/2021).

Appendix A. Supporting information

Supplementary data associated with this article can be found in the online version at doi:10.1016/j.jece.2023.111343.

References

[1] M. Ridley, G. Rao, F. Schilbach, V. Patel, Poverty, depression, and anxiety: causal evidence and mechanisms, Science 370 (6522) (2020) eaay0214, https://doi.org/10.1126/science.aay0214.
[2] N.M. Molenaar, A.M. Kamperman, P. Boyce, V. Bergink, Guidelines on treatment of perinatal depression with antidepressants: an international review, Aust. N. Z. J. Psychiatry 52 (4) (2018) 320–327, https://doi.org/10.1177/0004867418762057.
[3] A. Singh, D. Saidulu, A.K. Gupta, V. Kubsad, Occurrence and fate of antidepressants in the aquatic environment: Insights into toxicological effects on the aquatic life, analytical methods, and removal techniques, J. Environ. Chem. Eng. 10 (6) (2022), 109012, https://doi.org/10.1016/j.jece.2022.109012.
[4] OECD.Stat, Pharmaceutical Market: Pharmaceutical Consumption (Antidepressants). https://stats.oecd.org/Index.aspx?#.
[5] X.-T. Shao, S.-Y. Liu, Y.-T. Zhao, B. Jiang, J.-G. Lin, D.-G. Wang, Evaluation of eight psychoactive drugs used in Chinese cities by wastewater-based epidemiology, Sci. Total Environ. 855 (2023), 158982, https://doi.org/10.1016/j.scitotenv.2022.158982.
[6] L.E. Tomsone, I. Perkons, V. Sukajeva, R. Neilands, K. Kokina, V. Bartkevics, I. Pugajeva, Consumption trends of pharmaceuticals and psychoactive drugs in Latvia determined by the analysis of wastewater, Water Res. 221 (2022), 118800, https://doi.org/10.1016/j.watres.2022.118800.
[7] Md.J.S. Chaves, J. Kulzer, Pd.R. Pujol de Lima, S.C. Barbosa, E.G. Primel, Updated knowledge, partitioning and ecological risk of pharmaceuticals and personal care products in global aquatic environments, Environ. Sci.: Process. Impacts 24 (11) (2022) 1982–2008, https://doi.org/10.1039/D2EM00132B.

[8] P. Palma, S. Fialho, A. Lima, M.H. Novais, M.J. Costa, N. Montemurro, S. Pérez, M. L. de Alda, Pharmaceuticals in a Mediterranean Basin: The influence of temporal and hydrological patterns in environmental risk assessment, Sci. Total Environ. 709 (2020), 136205, https://doi.org/10.1016/j.scitotenv.2019.136205.

[9] M.P. Schlüsener, P. Hardenbicker, E. Nilson, M. Schulz, C. Viergutz, T.A. Ternes, Occurrence of venlafaxine, other antidepressants and selected metabolites in the Rhine catchment in the face of climate change, Environ. Pollut. 196 (2015) 247–256, https://doi.org/10.1016/j.envpol.2014.09.019.

[10] Commission implementing decision, (EU) 2022/1307 of 22 July 2022 establishing a watch list of substances for Union-wide monitoring in the field of water policy pursuant to Directive 2008/105/EC of the European Parliament and of the Council, Off. J. Eur. Union (2022).

[11] C. Belver, J. Bedia, A. Gómez-Avilés, M. Peñas-Garzón, J.J. Rodriguez, Chapter 22 - semiconductor photocatalysis for water purification, in: S. Thomas, D. Pasquini, S.-Y. Leu, D.A. Gopakumar (Eds.), Nanoscale Materials in Water Purification, Elsevier, 2019, pp. 581–651, https://doi.org/10.1016/B978-0-12-813926-4.00028-8.

[12] S.F. Ahmed, M. Mofijur, S. Nuzhat, A.T. Chowdhury, N. Rafa, M.A. Uddin, A. Inayat, T.M.I. Mahlia, H.C. Ong, W.Y. Chia, P.L. Show, Recent developments in physical, biological, chemical, and hybrid treatment techniques for removing emerging contaminants from wastewater, J. Hazard. Mater. 416 (2021), 125912, https://doi.org/10.1016/j.jhazmat.2021.125912.

[13] P.-S. Konstas, C. Kosma, I. Konstantinou, T. Albanis, Photocatalytic treatment of pharmaceuticals in real hospital wastewaters for effluent quality amelioration, Water 11 (10) (2019), https://doi.org/10.3390/w11102165.

[14] D. Lambropoulou, E. Evgenidou, V. Saliverou, C. Kosma, I. Konstantinou, Degradation of venlafaxine using TiO_2/UV process: Kinetic studies, RSM optimization, identification of transformation products and toxicity evaluation, J. Hazard. Mater. 323 (2017) 513–526, https://doi.org/10.1016/j.jhazmat.2016.04.074.

[15] N.F.F. Moreira, M.J. Sampaio, A.R. Ribeiro, C.G. Silva, J.L. Faria, A.M.T. Silva, Metal-free g-C_3N_4 photocatalysis of organic micropollutants in urban wastewater under visible light, Appl. Catal. B: Environ. 248 (2019) 184–192, https://doi.org/10.1016/j.apcatb.2019.02.001.

[16] N.F.F. Moreira, C.A. Orge, A.R. Ribeiro, J.L. Faria, O.C. Nunes, M.F.R. Pereira, A.M. T. Silva, Fast mineralization and detoxification of amoxicillin and diclofenac by photocatalytic ozonation and application to an urban wastewater, Water Res. 87 (2015) 87–96, https://doi.org/10.1016/j.watres.2015.08.059.

[17] F. Méndez-Arriaga, T. Otsu, T. Oyama, J. Gimenez, S. Esplugas, H. Hidaka, N. Serpone, Photooxidation of the antidepressant drug Fluoxetine (Prozac®) in aqueous media by hybrid catalytic/ozonation processes, Water Res. 45 (9) (2011) 2782–2794, https://doi.org/10.1016/j.watres.2011.02.030.

[18] P. Calza, C. Jiménez-Holgado, M. Coha, C. Chrimatopoulos, F. Dal Bello, C. Medana, V. Sakkas, Study of the photoinduced transformations of sertraline in aqueous media, Sci. Total Environ. 756 (2021), 143805, https://doi.org/10.1016/j.scitotenv.2020.143805.

[19] M. Sharma, A. Yadav, M.K. Mandal, K.K. Dubey, TiO_2 based photocatalysis: a valuable approach for the removal of pharmaceuticals from aquatic environment, Int. J. Environ. Sci. Technol. (2022), https://doi.org/10.1007/s13762-021-03894-y.

[20] J. Trawiński, R. Skibiński, Photolytic and photocatalytic degradation of the antipsychotic agent tiapride: Kinetics, transformation pathways and computational toxicity assessment, J. Hazard. Mater. 321 (2017) 841–858, https://doi.org/10.1016/j.jhazmat.2016.10.001.

[21] M. Inagaki, T. Tsumura, T. Kinumoto, M. Toyoda, Graphitic carbon nitrides (g-C_3N_4) with comparative discussion to carbon materials, Carbon 141 (2019) 580–607, https://doi.org/10.1016/j.carbon.2018.09.082.

[22] A. Torres-Pinto, C.G. Silva, J.L. Faria, A.M.T. Silva, The effect of precursor selection on the microwave-assisted synthesis of graphitic carbon nitride, Catal. Today 424 (2023), 113868, https://doi.org/10.1016/j.cattod.2022.08.010.

[23] R.A. Fernandes, M.J. Sampaio, J.L. Faria, C.G. Silva, Synthesis of vitamin B3 through a heterogeneous photocatalytic approach using metal-free carbon nitride-based catalysts, Molecules 27 (4) (2022), https://doi.org/10.3390/molecules27041295.

[24] C. Xing, G. Yu, T. Chen, S. Liu, Q. Sun, Q. Liu, Y. Hu, H. Liu, X. Li, Perylenetetracarboxylic diimide covalently bonded with mesoporous g-C_3N_4 to construct direct Z-scheme heterojunctions for efficient photocatalytic oxidative coupling of amines, Appl. Catal. B: Environ. 298 (2021), 120534, https://doi.org/10.1016/j.apcatb.2021.120534.

[25] C. Cheng, J. Shi, L. Mao, C.-L. Dong, Y.-C. Huang, S. Zong, J. Liu, S. Shen, L. Guo, Ultrathin porous graphitic carbon nitride from recrystallized precursor toward significantly enhanced photocatalytic water splitting, J. Colloid Interface Sci. 637 (2023) 271–282, https://doi.org/10.1016/j.jcis.2023.01.098.

[26] Z. Yu, Y. Li, A. Torres-Pinto, A.P. LaGrow, V.M. Diaconescu, L. Simonelli, M. J. Sampaio, O. Bondarchuk, I. Amorim, A. Araujo, A.M.T. Silva, C.G. Silva, J. L. Faria, L. Liu, Single-atom Ir and Ru anchored on graphitic carbon nitride for efficient and stable electrocatalytic/photocatalytic hydrogen evolution, Appl. Catal. B: Environ. 310 (2022), 121318, https://doi.org/10.1016/j.apcatb.2022.121318.

[27] Y. Cong, Y. Li, X. Wang, X. Wei, L. Che, S.-W. Lv, A newly-constructed double p-n heterojunction based on g-C_3N_4@NiO/Ni@MIL-101 ternary composite with enhanced photocatalytic performance for wastewater purification, Sep. Purif. Technol. 297 (2022), 121531, https://doi.org/10.1016/j.seppur.2022.121531.

[28] M.A. Barros, M.J. Sampaio, A.R. Ribeiro, C.G. Silva, A.M.T. Silva, J.L. Faria, Interactions of pharmaceutical compounds in water matrices under visible-driven photocatalysis, J. Environ. Chem. Eng. 9 (2) (2021), 104747, https://doi.org/10.1016/j.jece.2020.104747.

[29] J.C. Lopes, M.J. Sampaio, J.L. Faria, C.G. Silva, Synthesis and performance of a composite photocatalyst based on polyester-supported carbon nitride nanosheets for selective oxidation of anisyl alcohol, Surf. Interfaces 30 (2022), 101938, https://doi.org/10.1016/j.surfin.2022.101938.

[30] A.J. Kennedy, A.D. McQueen, M.L. Ballentine, L.R. May, B.M. Fernando, A. Das, K. L. Klaus, C.B. Williams, M.J. Bortner, Degradation of microcystin algal toxin by 3D printable polymer immobilized photocatalytic TiO_2, Chem. Eng. J. 455 (2023), 140866, https://doi.org/10.1016/j.cej.2022.140866.

[31] E. Valadez-Renteria, J. Oliva, V. Rodriguez-Gonzalez, Photocatalytic materials immobilized on recycled supports and their role in the degradation of water contaminants: a timely review, Sci. Total Environ. 807 (2022), 150820, https://doi.org/10.1016/j.scitotenv.2021.150820.

[32] Y. Gao, N. Yan, C. Jiang, C. Xu, S. Yu, P. Liang, X. Zhang, S. Liang, X. Huang, Filtration-enhanced highly efficient photocatalytic degradation with a novel electrospun rGO@TiO_2 nanofibrous membrane: implication for improving photocatalytic efficiency, Appl. Catal. B: Environ. 268 (2020), 118737, https://doi.org/10.1016/j.apcatb.2020.118737.

[33] Y. Wu, L. Lu, Y. Zhang, Z. Yuan, L. Yang, L. Wang, Y. Rao, A bioinspired cercosporin/polymethylmethacrylate photocatalyst with high efficiency for decontamination of pharmaceuticals and pathogens, J. Hazard. Mater. 419 (2021), 126555, https://doi.org/10.1016/j.jhazmat.2021.126555.

[34] A. Hu, X. Zhang, K.D. Oakes, P. Peng, Y.N. Zhou, M.R. Servos, Hydrothermal growth of free standing TiO_2 nanowire membranes for photocatalytic degradation of pharmaceuticals, J. Hazard. Mater. 189 (1) (2011) 278–285, https://doi.org/10.1016/j.jhazmat.2011.02.033.

[35] R.A. Osawa, B.T. Barrocas, O.C. Monteiro, M. Conceição Oliveira, M.H. Florêncio, Photocatalytic degradation of amitriptyline, trazodone and venlafaxine using modified cobalt-titanate nanowires under UV–Vis radiation: transformation products and in silico toxicity, Chem. Eng. J. 373 (2019) 1338–1347, https://doi.org/10.1016/j.cej.2019.05.137.

[36] R. Morsi, K.A. Al-Maqdi, M. Bilal, H.M.N. Iqbal, A. Khaleel, I. Shah, S.S. Ashraf, Immobilized soybean peroxidase hybrid biocatalysts for efficient degradation of various emerging pollutants, Biomolecules 11 (6) (2021), https://doi.org/10.3390/biom11060904.

[37] M.J. Sampaio, A.R.L. Ribeiro, C.M.R. Ribeiro, R.A. Borges, M.F. Pedrosa, A.M. T. Silva, C.G. Silva, J.L. Faria, A technological approach using a metal-free immobilized photocatalyst for the removal of pharmaceutical substances from urban wastewaters, Chem. Eng. J. 459 (2023), 141617, https://doi.org/10.1016/j.cej.2023.141617.

[38] O. Vieira, R.S. Ribeiro, M. Pedrosa, A.R. Lado Ribeiro, A.M.T. Silva, Nitrogen-doped reduced graphene oxide – PVDF nanocomposite membrane for persulfate activation and degradation of water organic micropollutants, Chem. Eng. J. 402 (2020), 126117, https://doi.org/10.1016/j.cej.2020.126117.

[39] L. Paredes, S. Murgolo, H. Dzinun, M.H. Dzarfan Othman, A.F. Ismail, M. Carballa, G. Mascolo, Application of immobilized TiO_2 on PVDF dual layer hollow fibre membrane to improve the photocatalytic removal of pharmaceuticals in different water matrices, Appl. Catal. B: Environ. 240 (2019) 9–18, https://doi.org/10.1016/j.apcatb.2018.08.067.

[40] N. Mokhtari, A.R. Solaimany Nazar, M. Farhadian, P. Eskandari, B. Jeon, Silver deposition on titanium oxide thin glass films for efficient visible light-induced photocatalytic removal of diphenhydramine and venlafaxine, Int. J. Environ. Sci. Technol. 19 (12) (2022) 12465–12476, https://doi.org/10.1007/s13762-022-04486-0.

[41] A. Dandapat, I. Horovitz, H. Gnayem, Y. Sasson, D. Avisar, T. Luxbacher, H. Mamane, Solar photocatalytic degradation of trace organic pollutants in water by Bi(0)-doped bismuth oxyhalide thin films, ACS Omega 3 (9) (2018) 10858–10865, https://doi.org/10.1021/acsomega.8b00759.

[42] N.-A.A.B. Taib, M.R. Rahman, D. Huda, K.K. Kuok, S. Hamdan, M.K.B. Bakri, M.R. M.B. Julaihi, A. Khan, A review on poly lactic acid (PLA) as a biodegradable polymer, Polym. Bull. 80 (2) (2023) 1179–1213, https://doi.org/10.1007/s00289-022-04160-y.

[43] D. da Silva, M. Kaduri, M. Poley, O. Adir, N. Krinsky, J. Shainsky-Roitman, A. Schroeder, Biocompatibility, biodegradation and excretion of polylactic acid (PLA) in medical implants and theranostic systems, Chem. Eng. J. 340 (2018) 9–14, https://doi.org/10.1016/j.cej.2018.01.010.

[44] X. Li, Y. Lin, M. Liu, L. Meng, C. Li, A review of research and application of polylactic acid composites, J. Appl. Polym. Sci. 140 (7) (2023), e53477, https://doi.org/10.1002/app.53477.

[45] P. Arnnok, R.R. Singh, R. Burakham, A. Pérez-Fuentetaja, D.S. Aga, Selective uptake and bioaccumulation of antidepressants in fish from effluent-impacted niagara river, Environ. Sci. Technol. 51 (18) (2017) 10652–10662, https://doi.org/10.1021/acs.est.7b02912.

[46] M.J. Lima, A.M.T. Silva, C.G. Silva, J.L. Faria, Graphitic carbon nitride modified by thermal, chemical and mechanical processes as metal-free photocatalyst for the selective synthesis of benzaldehyde from benzyl alcohol, J. Catal. 353 (2017) 44–53, https://doi.org/10.1016/j.jcat.2017.06.030.

[47] W.-J. Ong, L.-L. Tan, Y.H. Ng, S.-T. Yong, S.-P. Chai, Graphitic carbon nitride (g-C_3N_4)-based photocatalysts for artificial photosynthesis and environmental remediation: are we a step closer to achieving sustainability? Chem. Rev. 116 (12) (2016) 7159–7329, https://doi.org/10.1021/acs.chemrev.6b00075.

[48] S. Ayyaru, Y.-H. Ahn, Application of sulfonic acid group functionalized graphene oxide to improve hydrophilicity, permeability, and antifouling of PVDF nanocomposite ultrafiltration membranes, J. Membr. Sci. 525 (2017) 210–219, https://doi.org/10.1016/j.memsci.2016.10.048.

[49] S. Brunauer, P.H. Emmett, E. Teller, Adsorption of gases in multimolecular layers, J. Am. Chem. Soc. 60 (2) (1938) 309–319, https://doi.org/10.1021/ja01269a023.

[50] B.C. Lippens, J.H. de Boer, Studies on pore systems in catalysts: V. The t method, J. Catal. 4 (3) (1965) 319–323, https://doi.org/10.1016/0021-9517(65)90307-6.
[51] J. Tauc, Absorption edge and internal electric fields in amorphous semiconductors, Mater. Res. Bull. 5 (8) (1970) 721–729, https://doi.org/10.1016/0025-5408(70)90112-1.
[52] J. Liu, Origin of high photocatalytic efficiency in monolayer g-C_3N_4/CdS heterostructure: a hybrid DFT study, J. Phys. Chem. C. 119 (51) (2015) 28417–28423, https://doi.org/10.1021/acs.jpcc.5b09092.
[53] A. Torres-Pinto, I. Velo-Gala, S. Ribeirinho-Soares, O.C. Nunes, C.G. Silva, J. L. Faria, A.M.T. Silva, Novel photoelectrochemical 3D-system for water disinfection by deposition of modified carbon nitride on vitreous carbon foam, Environ. Res. 237 (2023), 117019, https://doi.org/10.1016/j.envres.2023.117019.
[54] C. Baumanis, D.W. Bahnemann, TiO_2 thin film electrodes: correlation between photocatalytic activity and electrochemical properties, J. Phys. Chem. C. 112 (48) (2008) 19097–19101, https://doi.org/10.1021/jp807655a.
[55] T. Giannakopoulou, I. Papailias, N. Todorova, N. Boukos, Y. Liu, J. Yu, C. Trapalis, Tailoring the energy band gap and edges' potentials of g-C_3N_4/TiO_2 composite photocatalysts for NO_x removal, Chem. Eng. J. 310 (2017) 571–580, https://doi.org/10.1016/j.cej.2015.12.102.
[56] D.R. Paul, R. Sharma, S.P. Nehra, A. Sharma, Effect of calcination temperature, pH and catalyst loading on photodegradation efficiency of urea derived graphitic carbon nitride towards methylene blue dye solution, RSC Adv. 9 (27) (2019) 15381–15391, https://doi.org/10.1039/C9RA02201E.
[57] R. Li, X. Cui, J. Bi, X. Ji, X. Li, N. Wang, Y. Huang, X. Huang, H. Hao, Urea-induced supramolecular self-assembly strategy to synthesize wrinkled porous carbon nitride nanosheets for highly-efficient visible-light photocatalytic degradation, RSC Adv. 11 (38) (2021) 23459–23470, https://doi.org/10.1039/D1RA03524J.
[58] Y. Zhang, J. Liu, G. Wu, W. Chen, Porous graphitic carbon nitride synthesized via direct polymerization of urea for efficient sunlight-driven photocatalytic hydrogen production, Nanoscale 4 (17) (2012) 5300–5303, https://doi.org/10.1039/C2NR30948C.
[59] Y. Cui, Y. Tang, X. Wang, Template-free synthesis of graphitic carbon nitride hollow spheres for photocatalytic degradation of organic pollutants, Mater. Lett. 161 (2015) 197–200, https://doi.org/10.1016/j.matlet.2015.08.106.
[60] P. Gibot, F. Schnell, D. Spitzer, Enhancement of the graphitic carbon nitride surface properties from calcium salts as templates, Microporous Mesoporous Mater. 219 (2016) 42–47, https://doi.org/10.1016/j.micromeso.2015.07.026.
[61] S. Kumar, A. Baruah, S. Tonda, B. Kumar, V. Shanker, B. Sreedhar, Cost-effective and eco-friendly synthesis of novel and stable N-doped ZnO/g-C_3N_4 core–shell nanoplates with excellent visible-light responsive photocatalysis, Nanoscale 6 (9) (2014) 4830–4842, https://doi.org/10.1039/C3NR05271K.
[62] J.L. Zimmerman, R. Williams, V.N. Khabashesku, J.L. Margrave, Synthesis of spherical carbon nitride nanostructures, Nano Lett. 1 (12) (2001) 731–734, https://doi.org/10.1021/nl015626h.
[63] Y. Sun, X. Wang, S. Xia, J. Zhao, Cu(II) adsorption on Poly(Lactic Acid) microplastics: significance of microbial colonization and degradation, Chem. Eng. J. 429 (2022), 132306, https://doi.org/10.1016/j.cej.2021.132306.
[64] J. Bian, C. Huang, R.-Q. Zhang, Graphitic carbon nitride film: an emerging star for catalytic and optoelectronic applications, ChemSusChem 9 (19) (2016) 2723–2735, https://doi.org/10.1002/cssc.201600863.
[65] E.M. Dias, K.C. Christoforidis, L. Francàs, C. Petit, Tuning thermally treated graphitic carbon nitride for H_2 evolution and CO_2 photoreduction: the effects of material properties and mid-gap states, ACS Appl. Energy Mater. 1 (11) (2018) 6524–6534, https://doi.org/10.1021/acsaem.8b01441.
[66] M. Medina-Llamas, A. Speltini, A. Profumo, F. Panzarea, A. Milella, F. Fracassi, A. Listorti, L. Malavasi, Preparation of heterojunctions based on $Cs_3Bi_2Br_9$ nanocrystals and g-C_3N_4 nanosheets for photocatalytic hydrogen evolution, Nanomaterials (2023).
[67] C. Amendola, M. Lacerenza, I. Pirovano, D. Contini, L. Spinelli, R. Cubeddu, A. Torricelli, R. Re, Optical characterization of 3D printed PLA and ABS filaments for diffuse optics applications, PLOS ONE 16 (6) (2021), e0253181, https://doi.org/10.1371/journal.pone.0253181.
[68] A. Torres-Pinto, H. Boumeriame, C.G. Silva, J.L. Faria, A.M.T. Silva, Boosting carbon nitride photoactivity by metal-free functionalization for selective H_2O_2 synthesis under visible light, ACS Sustain. Chem. Eng. 11 (3) (2023) 894–909, https://doi.org/10.1021/acssuschemeng.2c04512.
[69] Y. Yuan, L. Zhang, J. Xing, M.I.B. Utama, X. Lu, K. Du, Y. Li, X. Hu, S. Wang, A. Genç, R. Dunin-Borkowski, J. Arbiol, Q. Xiong, High-yield synthesis and optical properties of g-C_3N_4, Nanoscale 7 (29) (2015) 12343–12350, https://doi.org/10.1039/C5NR02905H.
[70] R.A. Fernandes, M.J. Sampaio, G. Dražić, J.L. Faria, C.G. Silva, Efficient removal of parabens from real water matrices by a metal-free carbon nitride photocatalyst, Sci. Total Environ. 716 (2020), 135346, https://doi.org/10.1016/j.scitotenv.2019.135346.
[71] L. Shi, L. Yang, W. Zhou, Y. Liu, L. Yin, X. Hai, H. Song, J. Ye, Photoassisted construction of holey defective g-C_3N_4 photocatalysts for efficient visible-light-driven H_2O_2 production, Small 14 (9) (2018) 1703142, https://doi.org/10.1002/smll.201703142.
[72] H. Zhang, L. Wang, J. Van herle, F. Maréchal, U. Desideri, Techno-economic comparison of 100% renewable urea production processes, Appl. Energy 284 (2021), 116401, https://doi.org/10.1016/j.apenergy.2020.116401.
[73] Y.F. Rao, W. Chu, Y.R. Wang, Photocatalytic oxidation of carbamazepine in triclinic-WO_3 suspension: role of alcohol and sulfate radicals in the degradation pathway, Appl. Catal. A: Gen. 468 (2013) 240–249, https://doi.org/10.1016/j.apcata.2013.08.050.
[74] X. Li, J. Yu, M. Jaroniec, Hierarchical photocatalysts, Chem. Soc. Rev. 45 (9) (2016) 2603–2636, https://doi.org/10.1039/C5CS00838G.